Drag enhancement and drag reduction in viscoelastic flow

Atul Varshney[1,2] and Victor Steinberg[1,3]
[1]*Department of Physics of Complex Systems, Weizmann Institute of Science, Rehovot 76100, Israel*
[2]*Institute of Science and Technology Austria, Am Campus 1, 3400 Klosterneuburg, Austria*
[3]*Racah Institute of Physics, Hebrew University of Jerusalem, Jerusalem 91904, Israel*

(Received 29 May 2018; published 15 October 2018)

Creeping flow of polymeric fluid without inertia exhibits elastic instabilities and elastic turbulence accompanied by drag enhancement due to elastic stress produced by flow-stretched polymers. However, in inertia-dominated flow at high Re and low fluid elasticity El, a reduction in turbulent frictional drag is caused by an intricate competition between inertial and elastic stresses. Here we explore the effect of inertia on the stability of viscoelastic flow in a broad range of control parameters El and (Re, Wi). We present the stability diagram of observed flow regimes in Wi-Re coordinates and find that the instabilities' onsets show an unexpectedly nonmonotonic dependence on El. Further, three distinct regions in the diagram are identified based on El. Strikingly, for high-elasticity fluids we discover a complete relaminarization of flow at Reynolds number in the range of 1 to 10, different from a well-known turbulent drag reduction. These counterintuitive effects may be explained by a finite polymer extensibility and a suppression of vorticity at high Wi. Our results call for further theoretical and numerical development to uncover the role of inertial effect on elastic turbulence in a viscoelastic flow.

DOI: 10.1103/PhysRevFluids.3.103302

I. INTRODUCTION

Long-chain polymer molecules in Newtonian fluid alter the rheological properties of the fluid; the relation between stress and strain becomes nonlinear. Moreover, polymers being stretched by a velocity gradient in shear flow engender elastic stress that modifies the flow via a feedback mechanism. It results in pure elastic instabilities [1,2] and elastic turbulence (ET) [3], observed at Re $\ll 1$ and Wi $\gg 1$. Here Re is the ratio of inertial to viscous stresses, $\mathrm{Re} = UD\rho/\eta$, and Wi defines the degree of polymer stretching $\mathrm{Wi} = \lambda U/D$, where U is the flow speed, D is the characteristic length scale, λ is the longest polymer relaxation time, and ρ and η are the density and dynamic viscosity of the fluid, respectively [4].

Elastic turbulence is a spatially smooth, random-in-time chaotic flow, whose statistical, mean, and spectral properties are characterized experimentally [3,5–11], theoretically [12,13], and numerically [14–17]. The hallmark of ET is a steep power-law decay of the velocity power spectrum with an exponent $|\alpha| > 3$ indicating that only a few modes are relevant to flow dynamics [3,5,12,13]. Further, an injection of polymers into a turbulent flow of Newtonian fluid at Re $\gg 1$ reduces the drag and also has a dramatic effect on the turbulent flow structures [18]. In recent investigations, a different state of small-scale turbulence associated with maximum drag reduction asymptotes was observed in a pipe flow at Re $\gg 1$ and Wi $\gg 1$. This state is termed elasto-inertial turbulence (EIT) and exhibits properties similar to ET despite the fact that it is driven by both inertial and elastic stresses and their interplay defines EIT properties [19–21]. Thus, the fundamental question arises how the inertial effect modifies ET in viscoelastic flow towards turbulent drag reduction.

Numerous studies were performed in various flow geometries to unravel the role of inertia on the stability of viscoelastic flow, however contradictory results were obtained. In Couette-Taylor

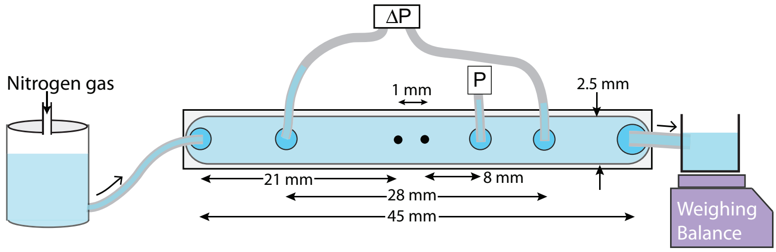

FIG. 1. Schematic of the experimental setup (not to scale). A differential pressure sensor, marked as ΔP, is used to measure pressure drop across the obstacles. An absolute pressure sensor, marked as P, after the downstream cylinder, is employed to obtain pressure fluctuations.

flow between two cylinders, the instability sets in at $\mathrm{Wi}_{\mathrm{tr}}$, which grows with the elasticity number El (=Wi/Re) saturating at sufficiently high El and reduces with increasing inertia [22–24]. In contrast, the onset of instability $\mathrm{Re}_{\mathrm{tr}}$ is almost constant at very low El and decreases with increasing El, in a rather limited range, in agreement with numerical simulations [25,26]. Recent experiments in the Couette-Taylor flow with both inner and outer co- and counterrotating cylinders at low El show a weak smooth dependence on El [27–29]. At moderate El, either stabilization or destabilization of the first bifurcation depending on co- or counterrotation of cylinders is found [27]. However, the general tendency in the dependences of the bifurcations on El reported in Refs. [22–24] was confirmed later in Refs. [27–29]. In contrast, a nonmonotonic dependence of the first bifurcation in a wall-bounded plane Poiseuille flow on El in its narrow range of low values was revealed in numerical simulations using the Oldroyd-B constitutive equation. The reduced solvent viscosity strongly modifies this effect: The smaller the polymer contribution to the viscosity, the less pronounced the effect [30]. In extensional viscoelastic flow [31], e.g., planar flow with an abrupt contraction and expansion, and in flow past a cylinder [32], the role of both elasticity and inertia was investigated in a narrow range of Re and Wi and for only three El values. In extensional flow, the onset of the elastic instability $\mathrm{Wi}_{\mathrm{tr}}$ turns out to be independent of Re in the range of 0.1–40 for three polymer solutions that correspond to $El = 3.8$, 8.4, and 89. However, in the case of flow past a cylinder [32] $\mathrm{Wi}_{\mathrm{tr}}$ decreases with increasing Re. Recent numerical studies [33] on two-dimensional viscoelastic flow past a cylinder reveal the phase diagram in (Wi, Re) coordinates and both drag enhancement and drag reduction (DR) were observed in the ranges Wi $\approx$ 0.2–10 and Re ≈ 0.1–10^5. Thus, despite extensive theoretical and experimental efforts, the influence of inertia on viscoelastic flow in a broad range of (Re, Wi) and El is still not understood and a stability diagram of different flow regimes is lacking.

Here we perform experiments, over a broad range of (Re, Wi) and El, in a channel flow of dilute polymer solution hindered by two widely spaced obstacles (see Fig. 1 for the experimental setup). Changing the solvent viscosity η_s by two orders of magnitude allows us to vary the elasticity number $El = \lambda(\eta_s)\eta_s/\rho D^2 \sim \eta_s^2/\rho D^2$ [34] by more than four orders of magnitude. Such an approach enables us to investigate the role of inertia in viscoelastic flow in different flow regimes in a wide range of (Re, Wi) and El.

The main feature of viscoelastic flow at Re $\ll 1$ between two widely spaced obstacles is an elastic wake instability in the form of quasi-two-dimensional counterrotating elongated vortices generated by a reversed flow [35]. The two vortices constitute two mixing layers with a nonuniform shear velocity profile filling the interobstacle space. A further increase of Wi leads to chaotic dynamics with properties similar to ET [11]. There are several reasons for the choice of the flow geometry. (i) Since the blockage ratio $D/w \ll 1$, the flow between the cylinders is unbounded, like "an island in a sea" of otherwise laminar channel flow, contrary to all previous wall-dominated flow geometries that were used to study ET (D and w are the cylinders' diameter and channel width, respectively) [3,5–9]. Therefore, we expect to observe mostly homogeneous, though anisotropic, flow closer to that considered in theory [12,13] and numerical simulations [14–16]. By employing unbounded flow, we concentrate on variation in the bulk flow structures due to polymer additives, which results in a significant frictional loss. (ii) Large Wi and Re can be reached in the same system to scan the range from ET to DR. (iii) Several techniques can be simultaneously employed to quantitatively characterize the flow.

II. EXPERIMENT

A. Experimental setup and materials

The experiments are conducted in a linear channel of $L \times w \times h = 45 \times 2.5 \times 1$ mm^3, shown schematically in Fig. 1. The fluid flow is hindered by two cylindrical obstacles of diameter $D = 0.30$ mm made of stainless steel separated by a distance of $e = 1$ mm and embedded at the center of the channel. Thus the geometrical parameters of the device are $D/w = 0.12$, $h/w = 0.4$, and $e/D = 3.3$. The channel is made from transparent acrylic glass [poly(methyl methacrylate)]. The fluid is driven by N_2 gas at a pressure up to $\sim$60 psi and injected via the inlet into a rectangular channel. As a fluid, a dilute polymer solution of high-molecular-weight polyacrylamide [PAAm, homopolymer of molecular weight $M_w = 18$ MDa (Polysciences)] at a concentration $c = 80$ ppm ($c/c^* \simeq 0.4$, where $c^* = 200$ ppm is the overlap concentration for the polymer used [34]) is prepared using water-sucrose solvent with a sucrose weight fraction varying from 0 to 60% (see Table 1 in [36]). The solvent viscosity η_s at 20 °C is measured in a commercial rheometer (AR-1000, TA Instruments). An addition of polymer to the solvent increases the solution viscosity η of about 30%. The stress-relaxation method [34] is employed to obtain λ; for $\eta_s = 0.1$ Pa s solution, λ is measured to be 10 ± 0.5 s. A linear dependence of λ on η was shown in Ref. [34].

B. Pressure measurements and imaging system

High-sensitivity differential pressure sensors (HSC series, Honeywell) of different ranges are used to measure the pressure drop ΔP across the obstacles and an additional absolute pressure sensor (ABP series, Honeywell) of different ranges is used to measure the pressure P fluctuations after the downstream cylinder at a sampling rate of 200 Hz, as shown schematically in Fig. 1. The accuracy of the pressure sensors used is $\pm 0.25\%$ full scale. We measure pressure drop for both solvent and polymer solution as a function of flow speed, and the difference between these two measurements provides information about the influence of polymers on the frictional drag.

The fluid exiting the channel outlet is weighed instantaneously $W(t)$ as a function of time t by a PC-interfaced balance (BA210S, Sartorius) with a sampling rate of 5 Hz and a resolution of 0.1 mg. The time-averaged fluid discharge rate $\bar{Q}$ is estimated as $\overline{\Delta W/\Delta t}$. Thus the flow speed is calculated as $U = \bar{Q}/\rho w h$. For flow visualization, the solution is seeded with fluorescent particles of diameter 1 μm (Fluoresbrite YG, Polysciences). The region between the obstacles is imaged in the midplane via a microscope (Olympus IX70), illuminated uniformly with light-emitting diode (Luxeon Rebel) at 447.5-nm wavelength and two CCD cameras attached to the microscope, (i) GX1920 Prosilica with a spatial resolution of 1936×1456 pixels at a rate of 50 frames/s (fps) and (ii) a high-resolution CCD camera XIMEA MC124CG with a spatial resolution of 4112×3008 pixels at a rate of 1 fps, are used to record the particles' streaks.

III. RESULTS

Frictional drag f for each El is calculated through the measurement of pressure drop across the obstacles ΔP (see Fig. 1) as a function of U and is defined as $f = 2D_h \Delta P/\rho U^2 L_c$; $D_h = 2wh/(w + h) = 1.43$ mm is the hydraulic radius and $L_c = 28$ mm is the distance between locations of ΔP measurement [35]. Figure 2 shows variation of f with Re for three El values and a sequence of transitions can be identified for each El. These transitions are further illustrated through a high-resolution plot of the normalized friction factor $f/f_{\rm lam}$ versus Re and Wi presented in the top and bottom insets of Fig. 2, respectively. Three flow regimes characterized by different scaling exponents

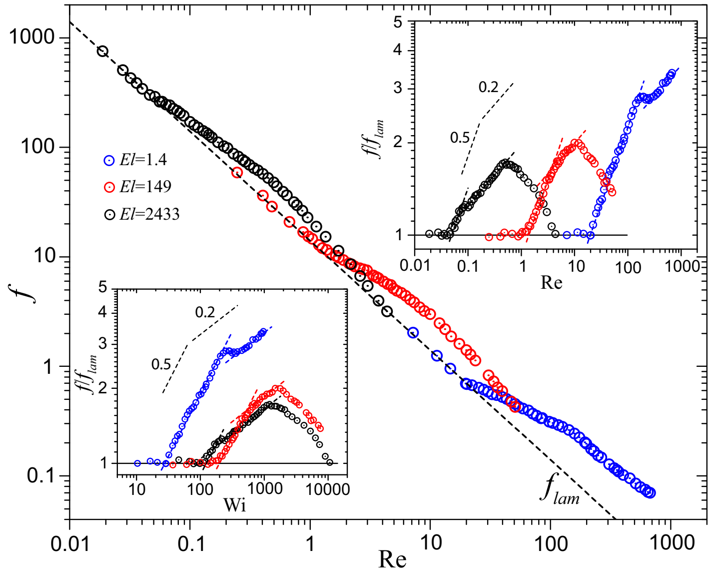

FIG. 2. Friction factor f versus Re for three values of El. The dashed line $f_{\mathrm{lam}} \sim 1/\mathrm{Re}$ represents the laminar flow. The top inset shows the normalized friction factor f/f_{lam} versus Re. The bottom inset shows the same data presented as f/f_{lam} versus Wi with the fits marked by dashed lines in two regions: $f/f_{\mathrm{lam}} \sim \mathrm{Wi}^{0.5}$ above the elastic instability and $f/f_{\mathrm{lam}} \sim \mathrm{Wi}^{0.2}$ in the ET regime. Note that the drag reduction for $El = 2433$ occurs at Re ≈ 0.5 and Wi ≈ 1216 and continues until the flow relaminarizes.

are identified. (i) The first drag enhancement above the elastic instability follows $f/f_{\mathrm{lam}} \sim \mathrm{Wi}^{0.5}$ for all values of El explored; for high El it is associated with a growth of two elongated vortices (or two mixing layers) [35]. (ii) Further drag enhancement at high El occurs due to ET [11] characterized by a steep algebraic decay both in the power spectra of velocity and pressure fluctuations with exponents greater than $\sim$3 (discussed in the following) and in intensive vorticity dynamics and a growth of average vorticity as $\bar{\omega} \sim \mathrm{Wi}^{0.2}$ and $f/f_{\mathrm{lam}} \sim \mathrm{Wi}^{0.2}$, typical for ET [11]. For low El, either a saturation or a reduction of the friction factor with Re or Wi marks the DR regime. (iii) For both high and intermediate El, the DR regime with decreasing f/f_{lam} at increasing Re or Wi is observed and at low El the drag enhancement is noticed. Another striking finding is a complete relaminarization of flow, i.e., 100% drag reduction, that occurs for $El = 2433$ (also for $El = 1070$ and 3704; data not shown), where f/f_{lam} returns to the laminar value at Re ≈ 4 (Wi $\approx 10^4$). With decreasing El, the transition points are shifted to a higher value of Re and Wi, and remarkably even at Re $\gg 1$ both drag enhancement and DR regimes can be recognized.

To elucidate further, the critical values of the respective transitions for each El is mapped in Re-El [Fig. 3(a)], Wi-El [Fig. 3(b)], and Wi-Re [Fig. 3(c)] coordinates. In the range explored for (Re, Wi), three different transitions are observed, which are associated with elastic instability, drag enhancement, and DR as shown in Figs. 3(a) and 3(b). These transitions persist for all elasticity values and the elastic instability occurs first, followed by the other two transitions. In addition, the complete flow relaminarization is observed only for $El = 1070$, 2433, and 3704. Interestingly, the sequence of DR and drag enhancement changes as El varies from low to high values; DR is followed by drag enhancement at low El and this sequence reverses at high El, as described above. This change in the sequence occurs in the intermediate range of elasticity at $El \sim 149$. Furthermore, three regions in Figs. 3(a)–3(c) can be identified based on variation of the critical values ($\mathrm{Re}_{\mathrm{tr}}$, $\mathrm{Wi}_{\mathrm{tr}}$) with El. For low elasticity ($El \leqslant 20$), $\mathrm{Re}_{\mathrm{tr}}$ is independent of El, while for high elasticity ($El \geqslant 300$), $\mathrm{Re}_{\mathrm{tr}}$ drops sharply with El. For intermediate elasticity ($20 \leqslant El \leqslant 300$), $\mathrm{Re}_{\mathrm{tr}}$

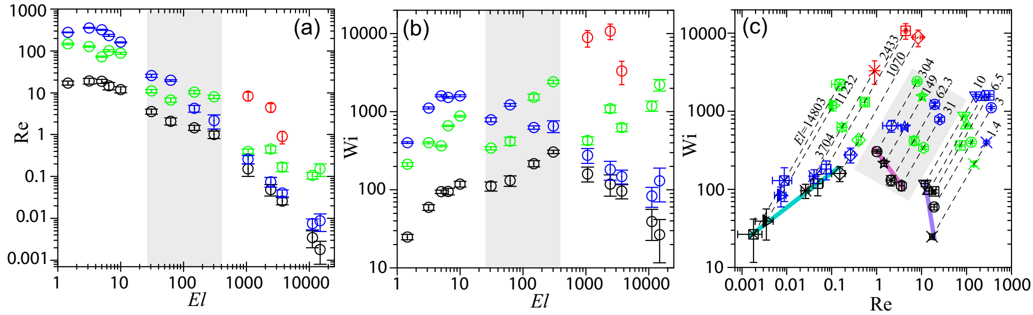

FIG. 3. Stability diagram of different flow regimes in (a) Re-El, (b) Wi-El, and (c) Wi-Re coordinates. The colors of the symbols signify different transitions: black, first elastic instability; green, DR; blue, drag enhancement; and red, flow relaminarization. The gray band in (a)–(c) indicates the region of intermediate El. Solid lines of different colors in (c) are used as a guide to the eye to track the transition in different regions.

shows a weak dependence on El [see Fig. 3(a)]. In Fig. 3(b) the dependence of $\mathrm{Wi}_{\mathrm{tr}}$ on El is nonmonotonic: a strong growth with El at low El, a sharp decrease at high El, and a gradual growth at intermediate El. The transitions are further mapped in the Wi-Re plane for different El to emphasize the role of inertia on the stability of a viscoelastic fluid flow. The same three regions are identified: At high El, $\mathrm{Wi}_{\mathrm{tr}}$ grows with $\mathrm{Re}_{\mathrm{tr}}$ with a stabilizing effect of inertia, at low El there is a steep drop of $\mathrm{Wi}_{\mathrm{tr}}$ with $\mathrm{Re}_{\mathrm{tr}}$, and in the intermediate region $\mathrm{Wi}_{\mathrm{tr}}$ decreases with increasing $\mathrm{Re}_{\mathrm{tr}}$ with the destabilizing effect of inertia [see Fig. 3(c)].

Long-exposure particle streak images in Fig. 4 illustrate the flow structures in three regions of elasticity and at different Re and Wi above the transitions' values (see also the corresponding movies SM1–SM9 in [36]). In low- and intermediate-elasticity regions, a large-scale vortical motion appears above the elastic instability; however, in DR and drag enhancement regimes, small-scale turbulent structures dominate and the large-scale vortical motion vanishes (top and middle panels in Fig. 4). In a high-elasticity region, e.g., $El = 14\,803$, an unsteady pair of vortices [35] spans the region between the obstacles (e.g., $\mathrm{Re} = 0.005$ and $\mathrm{Wi} = 74$) and at higher-Re small-scale vortices emerge with an intermittent and random dynamics (e.g., $\mathrm{Re} = 0.03$ and $\mathrm{Wi} = 444$) that constitutes the ET

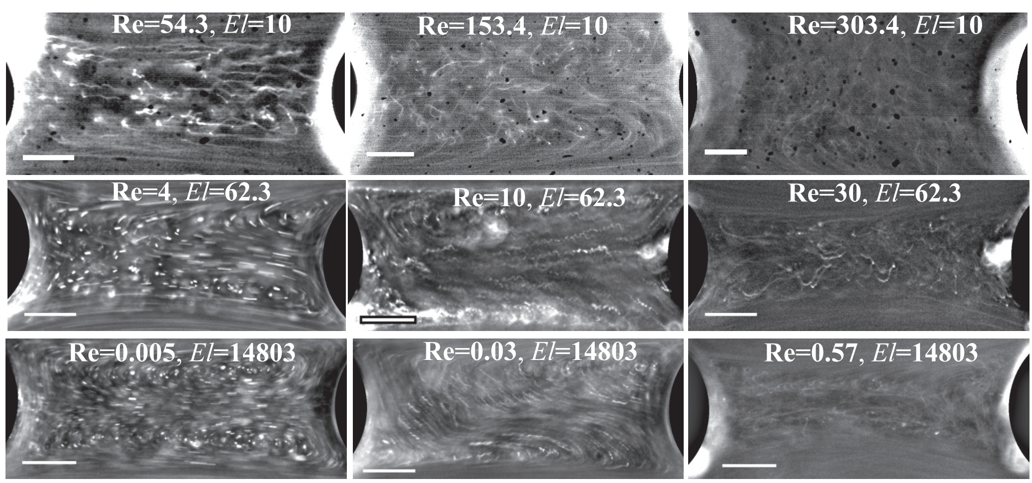

FIG. 4. Representative snapshots of flow structures in the three regions, above the transitions, at $El = 10$ (top panel), $El = 62.3$ (middle panel), and $El = 14\,803$ (bottom panel); see also the corresponding movies SM1–SM9 in [36]. The scale bars are 100 μm.

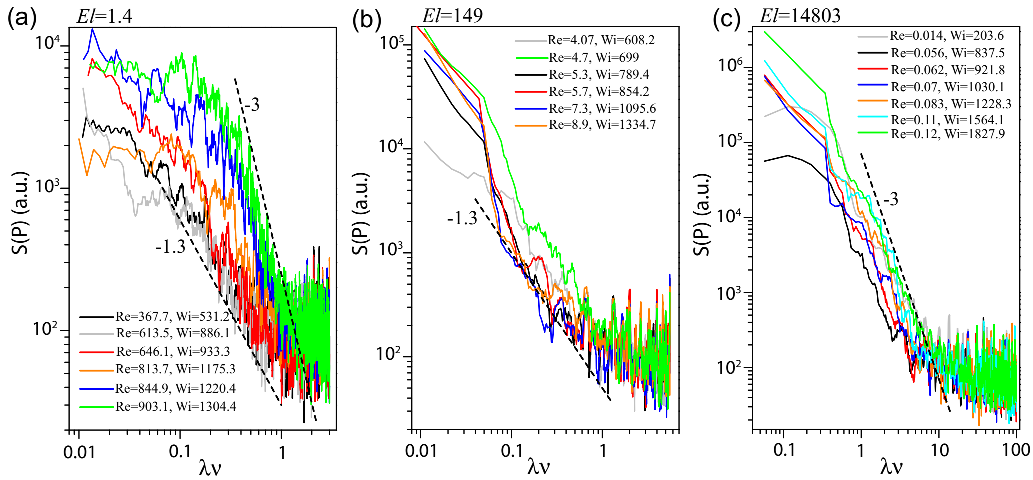

FIG. 5. Pressure power spectra $S(P)$ versus normalized frequency $\lambda\nu$ in the drag enhancement regime at various Re and Wi and in three regions of elasticity (a) $El = 1.4$, (b) $El = 149$, and (c) $El = 14\,803$. The dashed line shows power-law decay with an exponent β specified beside the line.

regime [11], whereas in the DR regime (e.g., Re $= 0.57$ and Wi $= 8438$) a much smoother spatial scale and less vortical motion are found (bottom panel of Fig. 4). However, a quantitative analysis of the velocity field at low and intermediate values of El requires serious technical effort and is beyond the scope of the present investigation.

Finally, we characterize the observed flow regimes through frequency power spectra of absolute pressure fluctuations for various Re and Wi in three regions of elasticity. The pressure spectra are presented as a function of normalized frequency $\lambda\nu$ to signify the timescales involved in flow with respect to λ. Figure 5 shows pressure power spectra $S(P)$ in the drag enhancement regime for three El values. For low elasticity, the $S(P)$ decay exponent β evolves from -1.3 to -3 with increasing Re and Wi and in the range of $\lambda\nu \sim 0.2$–1 [shown in Fig. 5(a) for $El = 1.4$]. It is worth noting that $\beta \approx -3$ is reached at the highest Re and Wi. In the intermediate range of elasticity, the exponent value $\beta = -1.3$ is obtained in the range of $\lambda\nu \sim 0.1$–1, the same as for low El [shown in Fig. 5(b) for $El = 149$], whereas for high El, $S(P)$ exhibits steep decay with $\beta \approx -3$ in a higher-frequency range $\lambda\nu \sim 1$–10 for all Re and Wi values for $El = 14\,803$ [Fig. 5(c)]. This value of β is one of the main characteristics of the ET regime [8,11]. The value $\lambda\nu = 1$ at high El is a relevant frequency to generate ET spectra with $\beta \approx -3$ at higher frequencies [8], as the stretching-and-folding mechanism of elastic stresses due to the velocity field redistributes energy across the scales [12,13]. Similar scaling of $S(P)$ is observed in numerical simulations in the dissipation range of the turbulent drag reduction regime [17]. For low El, the $S(P)$ decay at $\lambda\nu > 0.1$ up to 1 is caused by the inertial effect. In the drag reduction regime, $S(P)$ demonstrates completely different scaling behavior with $\lambda\nu$, shown in Fig. 6. For low El, one finds a steep decay of $S(P)$ at high frequencies $\lambda\nu \geqslant 1$ with a scaling exponent ~ -3.4 and a rather slow decay with an exponent between -0.5 and -1 at $\lambda\nu < 1$ [Fig. 6(a) for $El = 1.4$], in accord with numerical simulations [17]. For high El, the spectra $S(P)$ decay steeply at high frequency $\lambda\nu \sim 10$, and at low frequencies $0.1 < \lambda\nu \sim 10$ a slow decay with an exponent ~ -1 is observed [shown in Fig. 6(c) for $El = 14\,803$]. In the intermediate range of El, the decay exponent varies between -1.8 and -2.5 [shown in Fig. 6(b) for $El = 149$] in the frequency range $0.1 < \lambda\nu \sim 10$. To highlight the scaling dependences of $S(P)$ between different flow regimes in each El region, we present the same data in Fig. S1 in [36] for various Re and Wi and for three regions of El.

For comparison we present f as well as f/f_{lam} as a function of Re in the range between $\sim$6 and $\sim$900 for two Newtonian fluids, water ($\eta_s = 1$ mPa s) and a solution of 25% sucrose in water

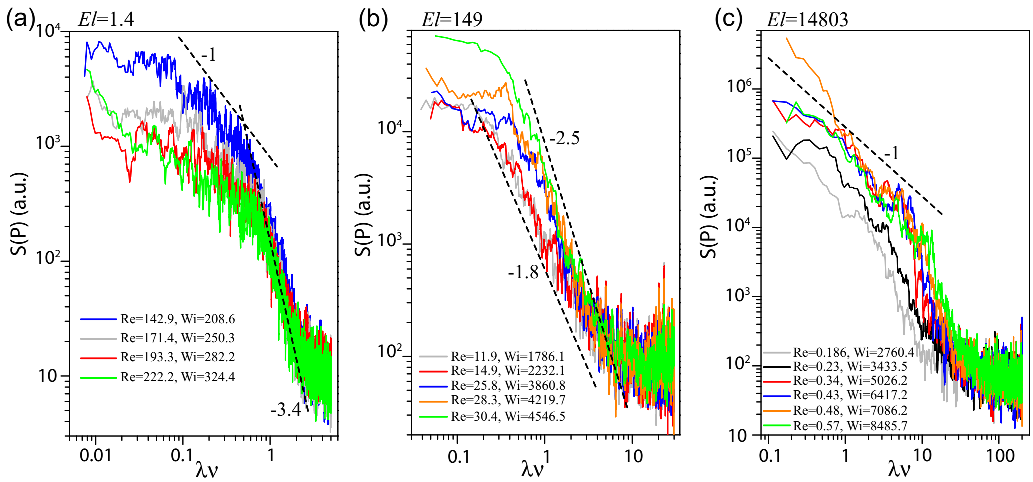

FIG. 6. Pressure power spectra $S(P)$ versus $\lambda\nu$ in the DR regime at various Re and Wi and in three regions of elasticity (a) $El = 1.4$, (b) $El = 149$, and (c) $El = 14\,803$. The dashed line shows power-law decay with an exponent specified beside the line.

($\eta_s = 3$ mPa s) (see Fig. S2 in [36]). The dependences of both f and $f/f_{\rm lam}$ on Re are smooth and growing at Re $\gtrsim 70$, which differs significantly from that found for polymer solutions at low El. It is also rather different from the dependence of f on Re in a channel flow past an obstacle, which is studied extensively. Thus, we can conclude that in viscoelastic flow, we observe inertia-modified elastic instabilities, contrary to inertial instabilities modified by elastic stress. This conclusion is further supported by the measurements of the power spectra of pressure fluctuations in a Newtonian fluid flow that exhibit a power-law exponent ~ -1.6 at high Re (see Fig. S3 in [36]), in contrast to those presented in Figs. 5 and 6.

IV. DISCUSSION AND CONCLUSION

Polymer degradation is often encountered under strong shear and in particular at high elongation rates due to velocity fluctuations at Re $\gg 1$ and Wi $\gg 1$ [37]. As a result of degradation, the influence of polymers on the flow becomes ineffective. To ensure that the drag enhancement and DR we observe in our experiments at Re $\geqslant 1$ are not the result of polymer degradation, we reuse the polymer solutions (after performing the experiment with two obstacles) in experiments on a channel flow with a single obstacle. Indeed, we observe elastic instability, drag enhancement, and DR with a single obstacle for $El = 14\,803$ (see, e.g., Fig. S4 in [36]). Moreover, the problem of polymer degradation was addressed in detail in our paper on turbulent drag reduction in a large-scale swirling flow experiment conducted at Re $\leqslant 2 \times 10^6$ [38]. It was pointed out that "the main technical achievement in the experiment was long term stability of polymers in turbulent flow that allowed us to take large data sets up to 10^6 data points for up to 3.5 hours at the highest Re without a sign of polymer degradation." Thus, we conclude that the observed flow regimes in our experiments are not caused by polymer degradation.

The presented results on the friction coefficient and the pressure power spectra obtained in a wide range of controlled parameters exhibit two remarkable features: (i) the presence of three flow regimes with distinctive and different scaling behavior in both $f/f_{\rm lam}$ and $S(P)$ and (ii) three regions on the stability diagrams in the planes of Re, Wi, and El parameters depending on the value of fluid elasticity. In spite of the fact that rather high values of Re are reached, inertial turbulence is not attained in the region between the obstacles and channel flow outside this region. As known from the literature, turbulence in a flow past an obstacle is attained at much higher Re [39].

The different scaling dependences of $S(P)$ in three flow regimes and in three regions of elasticity indicate the intricate interaction between elastic and inertial stresses. A two-way energy transfer between turbulent kinetic energy and elastic energy of polymers also results in a modification of the velocity spectra's scaling exponents at $\mathrm{Re} \gg 1$ [20,21]. The effect of inertia at $\mathrm{Re} \sim 100$ on the scaling behavior of velocity power spectra with the exponent $|\alpha| \approx 2.2$ instead of ~ 3.5 in pure ET was observed experimentally in the Couette-Taylor viscoelastic flow [6] and later confirmed numerically [40]. What is remarkable is that in the drag enhancement regime about the same scaling exponent $\beta \approx -3$ in $S(P)$ is found for low and high El at close values of Wi and a three order of magnitude difference in Re values. This indicates the elastic nature of drag enhancement regimes at both low and high El. Indeed, the scaling exponents of the pressure power spectrum decay for $El = 1.4$ [Fig. 5(a)] show $|\beta| \cong 3$ at $\mathrm{Re} >\sim 845$ and $\mathrm{Wi} >\sim 1220$. The observations of scaling $f/f_{\mathrm{lam}} \sim \mathrm{Wi}^{0.2}$, the exponent of the pressure spectrum decay $|\beta| \sim 3$, and the exponent of the velocity spectrum decay $|\alpha| \sim 3.5$ are characteristics of ET flow [11]. Thus, the drag enhancement regime in low-El regions is typical of ET.

A striking and unanticipated observation in the high-elasticity region is a significant DR and a complete flow relaminarization at $\mathrm{Wi} > 1000$ and $\mathrm{Re} \sim O(1)$ (see Figs. 2 and 3). The obtained result is different from turbulent DR observed at $\mathrm{Re} \gg 1$, where Reynolds stress exceeds the elastic stress prior to the onset of turbulent DR and becomes comparable to elastic stress at the onset. A similar effect of the saturation and even weak reduction of f/f_{lam} was observed and discussed in the planar geometry with an abrupt contraction and expansion of a microfluidic channel flow, where the saturation of f/f_{lam} at higher polymer concentrations c and even its reduction at lower $c < c^*$ were revealed in the range $0 < \mathrm{Wi} < 500$ for three polymer solutions of different polymer concentrations [31]. For the highest c, f/f_{lam} reached a value of ~ 3.5 at high Wi, in agreement with the early measurements in a pipe flow with an axisymmetric contraction and expansion at much lower $\mathrm{Wi} < 8$ [41].

To find a possible explanation of DR in a wide range of El and (Re, Wi), we discuss the effect in details. At low El between 1.4 and 31, either drag saturation or weak DR occurs just before the drag enhancement regime associated with ET and discussed above. It is worth mentioning that, due to the intricate interplay between elastic and inertial stresses, the strength of DR is a nonmonotonic function of El and depends on the relation between Wi and Re. The higher the Wi and the lower the Re, the more pronounced the DR regime at low El. The range of Re observed in the DR regime corresponds to the vorticity suppression by elastic stress generated by polymer additives injected into a Newtonian fluid flow [42–44], which is indeed confirmed by the snapshots at $El = 10$ and $\mathrm{Re} = 54$ and 153, shown in Fig. 4.

At high El in the range $149 < El < 14\,803$ and $\mathrm{Re} <\sim 70$, f/f_{lam} reduces significantly. However, the complete flow relaminarization is observed only at $El = 1070$, 2433, and 3704, where $\mathrm{Wi} \leqslant 10^4$ and $\mathrm{Re} < 10$. This means that high values of Wi and Re stabilize DR prior to the relaminarization due to finite polymer extensibility. The snapshot at $El = 14\,803$ and $\mathrm{Re} = 0.57$ in Fig. 4 shows a vorticity-free flow, in contrast to the snapshots at the same El and low Re. Thus, at $\mathrm{Re} \sim O(1)$ and high Wi, the inertial effects are negligible to suppress the growth of f/f_{lam}, whereas at $\mathrm{Re} \geqslant 70$ and intermediate values of Wi, the drag can be saturated, as seen, for example, at $El = 31$. As suggested in Ref. [31], the saturation of f/f_{lam} observed for high El is probably a consequence of polymer chains attaining their finite-extensibility limit at very-high-Wi values. Here we emphasize again that the DR observed at low El and high Re is not related to the turbulent drag reduction realized in a turbulent flow at higher values of Re than achieved in our experiment.

The theory of ET and the corresponding numerical simulations do not consider the inertial effects and their role in ET and therefore they are unable to explain the DR and flow relaminarization. Thus, the results reported call for further theoretical and numerical development to uncover inertial effects on viscoelastic flow in a broad range of (Re, Wi) and El.

ACKNOWLEDGMENTS

We thank Guy Han and Yuri Burnishev for technical support. We are grateful to Dr. Dongyang Li for his help in the measurements of the friction factor and the pressure spectra of Newtonian fluid flow. A.V. acknowledges support from the European Union's Horizon 2020 research and innovation program under the Marie Skłodowska-Curie Grant Agreement No. 754411. This work was partially supported by Israel Science Foundation (Grant No. 882/15) and Binational U.S.-Israel Foundation (Grant No. 2016145).

---

[1] R. G. Larson, Instabilities in viscoelastic flows, Rheol. Acta **31**, 213 (1992).
[2] E. S. G. Shaqfeh, Purely elastic instabilities in viscometric flows, Annu. Rev. Fluid Mech. **28**, 129 (1996).
[3] A. Groisman and V. Steinberg, Elastic turbulence in a polymer solution flow, Nature (London) **405**, 53 (2000).
[4] R. B. Bird, R. C. Armstrong, and O. Hassager, *Dynamics of Polymeric Liquids: Fluid Mechanics*, 2nd ed. (Wiley, New York, 1987), Vols. 1 and 2.
[5] A. Groisman and V. Steinberg, Efficient mixing at low Reynolds numbers using polymer additives, Nature (London) **410**, 905 (2001).
[6] A. Groisman and V. Steinberg, Elastic turbulence in curvilinear flows of polymer solutions, New J. Phys. **6**, 29 (2004).
[7] T. Burghelea, E. Segre, and V. Steinberg, Elastic turbulence in von Karman swirling flow between two disks, Phys. Fluids **19**, 053104 (2007).
[8] Y. Jun and V. Steinberg, Power and Pressure Fluctuations in Elastic Turbulence Over a Wide Range of Polymer Concentrations, Phys. Rev. Lett. **102**, 124503 (2009).
[9] Y. Jun and V. Steinberg, Elastic turbulence in a curvilinear channel flow, Phys. Rev. E **84**, 056325 (2011).
[10] L. Pan, A. Morozov, C. Wagner, and P. E. Arratia, Nonlinear Elastic Instability and the Transition to Turbulence at Low Reynolds Numbers, Phys. Rev. Lett. **110**, 174502 (2013).
[11] A. Varshney and V. Steinberg, Mixing layer instability and vorticity amplification in a creeping viscoelastic flow, Phys. Rev. Fluids (to be published).
[12] E. Balkovsky, A. Fouxon, and V. Lebedev, Turbulence of polymer solutions, Phys. Rev. E **64**, 056301 (2001).
[13] A. Fouxon and V. Lebedev, Spectra of turbulence in dilute polymer solutions, Phys. Fluids **15**, 2060 (2003).
[14] G. Boffetta, A. Celani, and S. Musacchio, Two-Dimensional Elastic Turbulence in Dilute Polymer Solutions, Phys. Rev. Lett. **91**, 034501 (2003).
[15] S. Berti, A. Bistagnino, G. Boffetta, A. Celani, and S. Musacchio, Small scale statistics of viscoelastic turbulence, Europhys. Lett. **76**, 63 (2006).
[16] S. Berti, A. Bistagnino, G. Boffetta, A. Celani, and S. Musacchio, Two-dimensional elastic turbulence, Phys. Rev. E **77**, 055306(R) (2008).
[17] T. Watanabe and T. Gotoh, Power-law spectra formed by stretching polymers in decaying isotropic turbulence, Phys. Fluids **26**, 035110 (2014).
[18] B. A. Toms, *Proceedings of the First International Congress of Rheology* (North-Holland, Amsterdam, 1949), Vol. 2, p. 135.
[19] D. Samanta, Y. Dubief, M. Holzner, C. Schäfer, A. N. Morozov, C. Wagner, and B. Hof, Elasto-inertial turbulence, Proc. Natl. Acad. Sci. USA **110**, 10557 (2013).
[20] Y. Dubief, V. E. Terrapon, and J. Soria, On the mechanism of elasto-inertial turbulence, Phys. Fluids **25**, 110817 (2013).
[21] V. E. Terrapon, Y. Dubief, and J. Soria, On the role of pressure in elasto-inertial turbulence, J. Turbul. **16**, 26 (2015).
[22] A. Groisman and V. Steinberg, Couette-Taylor Flow in a Dilute Polymer Solution, Phys. Rev. Lett. **77**, 1480 (1996).

[23] A. Groisman and V. Steinberg, Elastic vs inertial instability in a polymer solution flow, Europhys. Lett. **43**, 165 (1998).
[24] A. Groisman and V. Steinberg, Mechanism of elastic instability in Couette flow of polymer solutions: Experiment, Phys. Fluids **10**, 2451 (1998).
[25] Y. L. Joo and E. S. G. Shaqfeh, The effects of inertia on the viscoelastic Dean and Taylor-Couette flow instabilities with application to coating flow, Phys. Fluids A **4**, 2415 (1992).
[26] D. G. Thomas, B. Khomami, and R. Sureshkumar, Nonlinear dynamics of visco-elastic Taylor-Couette flow: Effect of elasticity on pattern selection, molecular conformation and drag, J. Fluid Mech. **620**, 353 (2009).
[27] C. Dutcher and S. Muller, The effects of drag reducing polymers on flow stability: Insights from the Taylor-Couette problem, Korea-Aust. Rheol. J. **21**, 223 (2009).
[28] C. Dutcher and S. Muller, Effects of weak elasticity on the stability of high Reynolds number co- and counter-rotating Taylor-Couette flows, J. Rheol. **55**, 1271 (2011).
[29] C. Dutcher and S. Muller, Effects of moderate elasticity on the stability of co- and counter-rotating Taylor-Couette flows, J. Rheol. **57**, 791 (2013).
[30] B. Sadanandan and R. Sureshkumar, Viscoelastic effects on the stability of wall-bounded shear flows, Phys. Fluids **14**, 41 (2002).
[31] L. E. Rodd, T. P. Scott, D. V. Boger, J. J. Copper-White, and G. H. McKinley, The inertio-elastic planar entry flow of low-viscosity elastic fluids in micro-fabricated geometries, J. Non-Newtonian Fluid Mech. **129**, 1 (2005).
[32] S. Kenney, K. Poper, G. Chapagain, and G.-F. Christopher, Large Deborah number flows around confined microfluidic cylinders, Rheol. Acta **52**, 485 (2013).
[33] Y. L. Xiong, C. H. Bruneau, and H. Kellay, Drag enhancement and drag reduction in viscoelastic fluid flow around a cylinder, Europhys. Lett. **91**, 64001 (2010).
[34] Y. Liu, Y. Jun, and V. Steinberg, Concentration dependence of the longest relaxation times of dilute and semi-dilute polymer solutions, J. Rheol. **53**, 1069 (2009).
[35] A. Varshney and V. Steinberg, Elastic wake instabilities in a creeping flow between two obstacles, Phys. Rev. Fluids **2**, 051301(R) (2017).
[36] See Supplemental Material at http://link.aps.org/supplemental/10.1103/PhysRevFluids.3.103302 for movies, figures, and a table.
[37] A. Gyr and H. W. Bewersdorf, *Drag Reduction of Turbulent Flows by Additives* (Kluwer, Dordrecht, 2003).
[38] Y. Burnishev and V. Steinberg, Influence of polymer additives on turbulence in von Karman swirling flow between two disks, II, Phys. Fluids **28**, 033101 (2016).
[39] P. K. Kundu and I. M. Cohen, *Fluid Mechanics*, 4th ed. (Elsevier, New York, 2008).
[40] N. Liu and B. Khomami, Elasticity induced turbulence in Taylor-Couette flow: Direct numerical simulation and mechanistic insight, J. Fluid Mech. **737**, R4 (2013).
[41] J. Rothstein and G. H. McKinley, The axisymmetric contraction-expansion: The role of extensional rheology on vortex growth dynamics and the enhanced pressure drop, J. Non-Newtonian Fluid Mech. **98**, 33 (2001).
[42] O. Cadot and M. Lebey, Shear instability inhibition in a cylinder wake by local injection of a viscoelastic fluid, Phys. Fluids **11**, 494 (1999).
[43] O. Cadot and S. Kumar, Experimental characterization of viscoelastic effects on two- and three-dimensional shear instabilities, J. Fluid Mech. **416**, 151 (2000).
[44] J. R. Cressman, Q. Baley, and W. I. Goldburg, Modification of a vortex street by a polymer additive. Phys. Fluids **13**, 867 (2001).